PCCP

ROYAL SOCIETY OF CHEMISTRY

PAPER

View Article Online
View Journal | View Issue

Cite this: *Phys. Chem. Chem. Phys.*, 2024, **26**, 27988

Dry desulphurisation of gas streams using KCC-1 mesoporous silica functionalised with deep eutectic solvents

Mohd Saiful Adli Azizman,[a] Muhammad Adli Hanif,[a] Naimah Ibrahim,*[ab] Ayu Wazira Azhari,[ab] Wan Khairunnisa Wan Ramli,[c] Aishah Abdul Jalil,[de] Nurul Sahida Hassan,[de] Fazilah Farhana Abdul Aziz[de] and Raja Nazrul Hakim Raja Nazri[f]

Received 18th August 2024,
Accepted 22nd September 2024

DOI: 10.1039/d4cp03248a

rsc.li/pccp

Sulphur dioxide, a toxic gas pollutant, is mainly generated by the combustion of fossil fuels and the smelting of sulphur-bearing mineral ores. Removal of SO_2 gas or desulphurisation can be accomplished in industries using a variety of processes; the most efficient is wet flue gas desulphurisation (FGD). However, wet FGD has challenges, such as the requirement for wastewater treatment, excessive water usage, and the necessity for chloride protective coating. Despite having a lesser adsorption capacity than wet FGD, dry FGD can efficiently remove SO_2 from the effluent gas stream and avoid the issues associated with wet FGD, provided that the sorbents are modified and regenerable. An alternative dry desulphurisation strategy by using fibrous mesoporous silica (KCC-1) modified with deep eutectic solvents (DES), choline chloride–glycerol (DES1) and choline chloride–ethylene glycol (DES2) is studied in this paper. KCC-1 modified with DES1 is found to increase SO_2 adsorption capacity to 4.83 mg g^{-1}, which is 1.73 times greater than unmodified KCC-1 and twice higher than KCC-1 modified with DES2 attributed to the sorbent's high porosity. Increasing reaction temperature and SO_2 concentration reduce the adsorption capacity to 1.73 mg g^{-1} and 2.73 mg g^{-1}, respectively. The Avrami kinetic model and the Toth isotherm model best reflect SO_2 adsorption on the modified KCC-1, indicating that SO_2 molecules are adsorbed exothermically in multilayer adsorption on a heterogeneous surface through a combination of physical and chemical processes. The higher SO_2 adsorption capacity of the modified KCC-1 suggests that choline chloride–glycerol can provide additional sites for SO_2 adsorption in dry FGD technology.

1. Introduction

Clean air is vital for all living things in order to sustain human health, protect ecosystems, and help preserve building structures. Unfortunately, fossil fuel utilisation in road transportation, power generation and industrial activities produces reactive air pollutants, including nitrogen oxides (NO_x), carbon monoxide (CO), particulate matter (PM) and sulphur dioxide (SO_2) that pose a significant threat to human health and the environment.[1] While CO has the most immediate impact on health due to its capability to bind in red blood cells and rapidly reduce oxygen delivery[2] and PM exposure has the most significant long-term health risks for cardiovascular disease and cancer,[3] SO_2 primarily affects the respiratory systems, causing irritation, coughing and asthma. In addition, SO_2 also contribute to the formation of acid rain, harming forests, reducing soil fertility and damaging aquatic ecosystems.[4]

Since the late 1960s, flue gas desulphurisation (FGD) technology has reduced emissions from coal-fired power plants. FGD systems typically comprise a vertical, cylindrical tower or column in which the solvent is brought into contact with the pollutants to be removed from the exhaust gas. These systems are frequently employed in industry for gas stream purification and separation, product recovery, and pollution management.

[a] *Faculty of Civil Engineering & Technology, Universiti Malaysia Perlis, Arau, Perlis, 02600, Malaysia. E-mail: naimah@unimap.edu.my*
[b] *Centre of Excellence for Water Research and Environmental Sustainability Growth (WAREG), Universiti Malaysia Perlis, Arau, Perlis, 02600, Malaysia*
[c] *Faculty of Chemical Engineering & Technology, Universiti Malaysia Perlis, Arau, Perlis, 02600, Malaysia*
[d] *Faculty of Chemical and Energy Engineering, Universiti Teknologi Malaysia, Johor Bahru, Johor, 81310, Malaysia*
[e] *Centre of Hydrogen Energy, Institute of Future Energy, 81310, UTM, Johor Bahru, Johor, Malaysia*
[f] *Universiti Kuala Lumpur, Branch Campus Malaysian Institute of Chemical and Bioengineering Technology, Lot 1988, Kawasan Perindustrian Bandar Vendor, Alor Gajah, Melaka, 78000, Malaysia*

Wet limestone, seawater-based, ammonia-based, and dry FGD are common methods used in power stations to reduce SO_2 emissions. These methods are proven technologies and commercially available. The capacity to remove sulphur, dependability, spatial requirements, and reagent availability are the primary technical, economic, and commercial variables influencing the choice of a suitable FGD technology.[5] Wet FGD systems generally achieve higher SO_2 removal efficiency (exceeding 90%) than dry FGD systems (approximately 80%). However, the large amount of wastewater produced by wet FGD systems must be treated before disposal, requiring additional cost and time.[6,7]

Among the variety of sorbents in dry FGD, activated carbon is a commonly studied material which can be derived from various carbonaceous sources like agricultural wastes. Unfortunately, the application of activated carbon in up-scaled SO_2 treatment is frequently limited by high flue gas temperatures and acidic gas compositions.[8] Mesoporous silica (MS) based sorbents offer more extensive applications, including in medicine delivery, wastewater treatment, indoor air purification, catalysis, and SO_2 removal from flue gas.[9] MS are superior because of their unique features, which include organised pore architectures, high specific surface areas, and the ability to be synthesised in various morphologies, including spheres, rods, discs, powders, *etc.*

One of the newest members of the MS materials group, KAUST Catalyst Centre-1 (KCC-1), was initially synthesised in 2010 by Polshettiwar *et al.*[10] In contrast to the conventional MS materials such as Fudan University-12 (FDU-12), Korea Institute of Science and Technology-5 and 6 (KIT-5, KIT-6), Santa Barbara Amorphous-15 and 16 (SBA-15, SBA-16), Mobil Composition of Matter-41 and 48 (MCM-41, MCM-48), KCC-1 has concentric and regular fibres that developed radially from the centre of the silica spheres to the outside of the spheres, which accounts for its high surface area.[11,12] As a result, KCC-1 could be an excellent alternative for catalysis applications and adsorption that require easily accessible active sites.[12–15] Silica-based sorbents require modification to enhance removal efficiencies and improve catalytic activities, as limited active sites will reduce their accessibility when significant mass transport is vital.[16] Modification of silica-based materials has been shown to improve the adsorption activity of the sorbents in a recent work by Lai *et al.*[17]

On the other hand, the use of deep eutectic solvent (DES) for CO_2 capture and SO_2 sequestration has also grown in interest.[18] DES has a high distribution coefficient of solutes, which means it is particularly efficient in storing solutes with properties and behaviours similar to ionic liquids (ILs). DES has been widely employed in organic synthesis, metal electrodepositions and extractions, and CO_2 absorptions due to its low cost, low volatility, non-toxicity and ease of synthesis. Yang *et al.*[19] reported that DES achieves high SO_2 sorption capacity through significant charge transfer interactions between chloride anion and SO_2 molecules. Furthermore, the interaction may be tuned to control SO_2 desorption, so that the sorbent can be cycled multiple times. In addition, DES is advantageous in FGD applications due to its good thermal stability and the ability to maintain stability.[13] Motivated by the excellent properties of KCC-1 and DES, the suitability of KCC-1 modified with DES for SO_2 removal was investigated in this work.

2. Materials and methods

2.1 Materials

2.1.1 Gases and chemicals. Synthetic gases, 0.3% sulphur dioxide/nitrogen (SO_2/N_2) mixture and purified nitrogen (N_2) were supplied by Linde, Malaysia. Meanwhile, choline chloride ($\geq$98%), glycerol ($\geq$99%) and ethylene glycol ($\geq$99%) were from Sigma-Aldrich, Germany.

2.1.2 KCC-1 mesoporous silica. KCC-1 mesoporous silica was obtained from Universiti Teknologi Malaysia (UTM) in powder form and used as received. The synthesis of KCC-1 has been explained in other work.[20]

2.2 Methods

2.2.1 Synthesis of deep eutectic solvent. Deep eutectic solvent solutions preparation was adopted from previous studies using the heating method.[21,22] The KCC-1 samples modified with choline chloride mixed with glycerol were denoted as DES1 and choline chloride mixed with ethylene glycol as DES2, respectively. To prepare the materials, choline chloride was first oven-dried at 80 °C for 12 hours due to its hygroscopic nature. Choline chloride, a hydrogen bond acceptor (HBA), was then mixed with a hydrogen bond donor (HBD), either glycerol or ethylene glycol, to produce DES1 and DES2 samples, respectively, at the molar ratio of 1 : 2 (HBA : HBD) by stirring for 60 min at 60 °C (with glycerol) and 70 °C (with ethylene glycol). This specific ratio was selected based on preliminary findings indicating optimal performance with minimised chemical usage. A ratio of 1 : 1 is inapplicable as the produced DES will self-crystallise during storage. The mixtures were agitated until clear and homogeneous. Afterwards, the mixtures were allowed to cool to room temperature and then stored in sealed vials, kept in a desiccator.

2.2.2 KCC-1 modification. KCC-1 was modified with DES solutions using the incipient wetness impregnation method.[23] The process involved adding DES solutions into beakers containing KCC-1 samples in powder form and mixing until the samples appeared visibly wet but without excess liquid. The samples were then oven-dried for 12 hours at 110 °C before being calcined for 6.5 hours at 550 °C. The resulting powders, designated as KCC-1/DES1 and KCC-1/DES2 depending on the respective DES mixtures, were stored in a desiccator until further use.

2.2.3 SO_2 removal study. A preliminary SO_2 breakthrough study was conducted to compare SO_2 removal efficiency between fresh and DES-modified KCC-1. For this purpose, a 0.3 g sample (with an average bed height of 20 mm) was placed in the centre of a quartz tube reactor (ID = 8.8 mm, OD = 12.7 mm), with quartz wool filling the empty spaces.[24] The reactor was positioned inside a tubular furnace equipped with a programmable controller (Vecstar VCTF SP, United Kingdom). The sorbent bed was degassed with 100 mL min^{-1} N_2 flow at

150 °C for 60 min to remove residual moisture and air. After that, the reactor was left to cool to 40 °C. The SO_2 breakthrough experiment was carried out with a 200 mL min^{-1} flow of 1500 ppm SO_2 gas balanced in N_2, and the concentration of exit gas was continuously monitored using a Testo 340 gas analyser (Testo, Germany) until the sorbent bed achieved at least 95% saturation. The flow rate was chosen to achieve a high gas hourly space velocity (GSHV) of 25 000 h^{-1}, characteristic of an exhaust gas condition.

In this study, the breakthrough point was considered achieved once the gas analyser measured 5% of the initial SO_2 concentration in the exit gas stream. To ease comparison with samples that took too long to reach complete saturation, the capacity of SO_2 removal was computed at a fractional concentration (C/C_0) equal to 0.95 using eqn (1), assuming all samples have reached bed saturation. C and C_0 are the SO_2 concentrations at time t and initial SO_2 concentration (mg L^{-1}), respectively; y_t is the gas molar fraction, Q_f is the gas flow rate (L min^{-1}), and m_c is the mass of the sorbent bed (g).

$$q = \frac{C_0 Q_f y_t}{m_c} \int_0^\infty \left(-\frac{C}{C_0}\right) dt \quad (1)$$

An important metric in fixed bed adsorption is the mass transfer zone (MTZ), which quantifies the efficiency of sorbent utilisation, where adsorbate mass transfer occurs, resulting in adsorption. The MTZ started to move from the inlet to the outlet as soon as the gas supply was activated and continued to progress until saturation was achieved. The MTZ was computed using eqn (2), where H is the sorbent length in cm, while t_b and t_s are the breakthrough and saturation time in minutes, respectively.

$$\mathrm{MTZ} = H\left(1 - \frac{t_b}{t_s}\right) \quad (2)$$

The samples were also tested under different operating conditions, *i.e.*, reaction temperatures and inlet concentrations. In the former conditions, the reactor was set to achieve the desired reaction temperatures (40, 80 or 120 °C) at a fixed SO_2 concentration of 1500 ppm, while in the latter, the reactor was cooled to a constant reaction temperature of 40 °C and the concentration of SO_2 gas stream was varied from 1500 to 2000 ppm.

2.2.4 Sample characterization. The characterisation of fresh and modified samples was conducted both physically and chemically. The surface morphology was assessed using a Zeiss Leo 1525 field emission scanning electron microscope (FESEM) with Type II secondary electron image (SEI) at a magnification of ×50 000. Meanwhile, Fourier Transform Infrared Spectroscopy (FTIR) *via* attenuated total reflection (ATR) was used to examine the surface chemistry of the samples using a Frontier PerkinElmer instrument, with polystyrene film NIST as the verification material. The surface area and porosity of fresh and modified KCC-1 were determined through N_2 adsorption–desorption using Micromeritics 3Flex at −196 °C. Before measurement, the samples were degassed at 150 °C for 1 hour. The surface area, average pore size and pore volume of all samples were determined by Brunauer–Emmett–Teller (BET) analysis and the Medek model as well as the adsorbed N_2 volume calculation at standard temperature and pressure (STP), respectively.

2.2.5 Kinetic study. Adsorption kinetics provides insights into the sorption mechanism and the rate of the adsorption process, which involves adsorbent surface reaction, diffusion, and mass transfer (*i.e.*, external mass transfer at the active centres over emergence (chemical or physical bonds) of the adsorbate at the adsorbent pores, the diffusion film and diffusion within the adsorbent particles).[25,26] The adsorption capacities obtained at varying reaction temperatures were fitted to nonlinear pseudo-first-order (P1st), pseudo-second-order (P2nd) and Avrami kinetic models as shown in eqn (3)–(5), respectively:

$$q_t = q_e[1 - \exp(-K_1 t)] \quad (3)$$

$$q_t = \frac{K_2 q_e^2 t}{(1 + K_2 q_e t)} \quad (4)$$

$$q_t = q_e[1 - \exp(-K_3 t^{N_A})] \quad (5)$$

where q_t is the adsorption capacity (mg g^{-1}) at time t (minutes), and q_e is the equilibrium capacity of adsorption (mg g^{-1}). The P1st and P2nd reaction rate constants are K_1 and K_2, respectively, while the Avrami constant and time exponent associated with the change in the adsorption mechanism are denoted by K_3 and N_A, respectively.

2.2.6 Isotherm study. Isotherms are typically used to characterise and investigate the most significant features of an adsorption, including the quantitative distribution of adsorbate (bulk solution) and the adsorbent, as well as adsorption capacity, mechanism and affinity. The nonlinear Langmuir, Freundlich and Toth coefficients were calculated from the adsorption data collected at varying SO_2 concentrations, using eqn (6)–(8), respectively.

$$q_t = \frac{K_L q_m C_e}{(1 + C_e K_L)} \quad (6)$$

$$q_t = K_F C_e^{1/n} \quad (7)$$

$$q_t = \frac{K_T q_m C_e}{\left[1 + (C_e K_T)^{N_T}\right]^{1/N_T}} \quad (8)$$

The Langmuir reaction rate constant is represented by K_L (mg g^{-1}), and the maximum adsorption capacity is denoted as q_m (mg g^{-1}). C_e *vs.* q_e describes the nonlinear isotherm plots, where C_e (mg L^{-1}) represents the equilibrium SO_2 concentration and q_e (mg g^{-1}) represents the amount of adsorbate adsorbed by the sorbent at equilibrium (per unit mass). As C_e reflects the amount of SO_2 molecules not adsorbed by the adsorbent, the value of C_e is directly taken from the analyser and converted to the appropriate units. The value of q_e is calculated using eqn (1) under equilibrium conditions.

Freundlich's reaction rate constant is denoted as K_F (L mg^{-1}), while the adsorption affinity is represented by $1/n$ (dimensionless). On the other hand, K_T (mg g^{-1}) and N_T (mg g^{-1}) are Toth rate and isotherm constants, respectively.

The adsorption process is evaluated based on the value of $1/n$. A $1/n < 1$ indicates chemisorption, or alignment with the conventional Langmuir isotherm, whereas a $1/n > 1$ indicates cooperative adsorption. The Toth equation describes a heterogeneous, multilayer adsorption system and serve as a specialised form of Langmuir isotherm with minimal validity. The system heterogeneity is represented by the parameter N_T. The further its deviation from unity, the greater the heterogeneity within the system.

2.2.7 Thermodynamic study. The adsorption thermodynamic study was conducted to elucidate the thermodynamic characteristics, which convey information about the adsorption behaviour. Eqn (9) below is the thermodynamic definition of chemical equilibrium where ΔG° is the change in Gibbs free energy, ΔS° entropy change, ΔH° enthalpy change, T temperature in Kelvin, R: 8.314 J K^{-1} mol^{-1} is the universal gas constant, and K_e° (dimensionless) is the adsorption thermodynamic equilibrium constant.[27]

$$K_e^\circ = \exp\left[\left(\frac{\Delta S^\circ}{R}\right) - \left(\frac{\Delta H^\circ}{R}\right) \times \frac{1}{T}\right] \quad (9)$$

3. Results and discussion

3.1 DES synthesis

After heating, the initial attempt to prepare the DES solution using a 1 : 1 molar ratio of HBA to HBD resulted in a colourless, homogeneous liquid. However, a white precipitate formed in both DES1 and DES2 mixtures after cooling to room temperature. As noted by Manurung *et al.*, the formation of precipitates in a DES mixture can be attributed to excess halide anions, which can occur when the concentration of the HBA is insufficient to form hydrogen bonds with all the halide anions.[28] Furthermore, excess salts may also lead to an increase in the freezing point of the mixture, resulting in precipitation, as mentioned by Makos *et al.* and Qin *et al.*, highlighting that the molar ratio of the HBA to HBD significantly influences the freezing point of the DES.[29,30] By adjusting the molar ratio to 1 : 2, a clear and homogeneous DES solution was achieved at room temperature, indicating a more balanced interaction between the HBA and HBD components, as shown in Fig. 1(a).

3.2 KCC-1 optimization and characterization

The SO_2 breakthrough study produced a breakthrough-time curve (C/C_0 *versus* t), where C_0 is the initial concentration (ppm) of SO_2 passed through the adsorbent bed and C is the outlet concentration (ppm) recorded by the gas analyser. Both fresh and DES-modified KCC-1 samples (KCC-1/DES1 and KCC-1/DES2) were screened, and the sample exhibiting the highest adsorption capacity was selected for further optimisation by varying reaction temperatures and inlet concentrations. Fig. 2 shows the breakthrough curves of all three samples under 200 mL min^{-1} flow of 1500 ppm SO_2, while Table 1 summarises the adsorption capacity and breakthrough data for these samples.

Table 1 and Fig. 2 show that KCC-1/DES1 has the longest adsorption breakthrough time of 91 seconds compared to the other samples under the same experimental conditions. On the other hand, KCC-1/DES2 has a faster breakthrough time than fresh KCC-1 and KCC-1/DES1, respectively, which is less preferred, as the slower the breakthrough time, the longer the adsorption bed can serve.

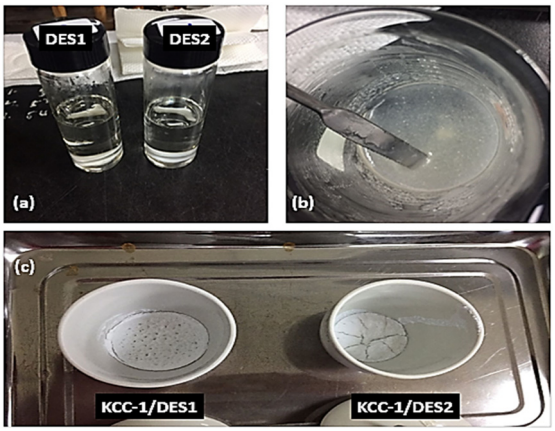

Fig. 1 Physical appearance: (a) DES solution at room temperature, (b) post-mixing of modified catalyst and (c) post-calcination of modified KCC-1.

The breakthrough investigation of fresh and modified KCC-1 samples reveals SO_2 adsorption capacities (at C/C_0 = 0.95) ranging between 2.41 and 4.84 mg g^{-1}. KCC-1/DES1 exhibits the highest SO_2 adsorption capacity, which is 1.73 times higher than that of fresh KCC-1 and 2 times higher than KCC-1/DES2. The results also show that fresh KCC-1 has the lowest MTZ of 87.21% compared to KCC-1/DES1 and KCC-1/DES2, with MTZ values of 92.17 and 87.95%, respectively. A low MTZ is theoretically caused by a high flow rate, which shortens the time it takes for the adsorbate to diffuse into the pores of the sorbent materials as the adsorbate solution (or gas mixture in this case) leaves the column before reaching equilibrium, causing breakthrough time to appear relatively faster.[31]

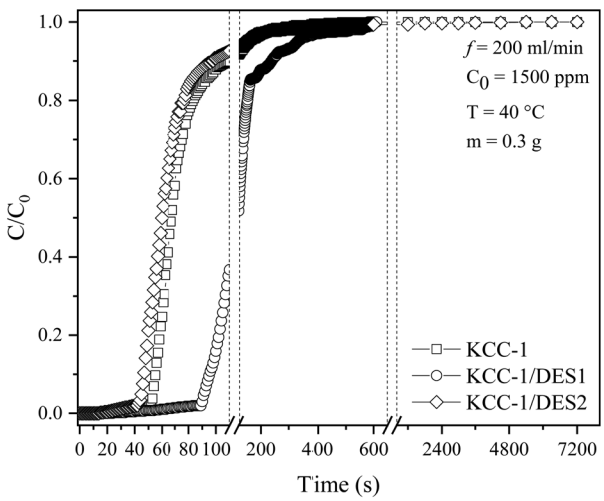

Fig. 2 SO_2 breakthrough curves of fresh KCC-1 and DES-modified KCC-1.

Table 1 Summary of SO_2 removal performance by fresh KCC-1 and DES-modified KCC-1

Sample	Breakthrough time at C/C_0 = 0.05 (s)	Time at C/C_0 = 0.95 (s)	MTZ (%)	Adsorption capacity at C/C_0 = 0.95 (mg SO_2 per g sample)
KCC-1	54	159	87.21	2.79
KCC-1/DES1	91	332	92.17	4.84
KCC-1/DES2	46	144	87.95	2.41

According to recent studies in gas adsorption, choline chloride-based DES is deemed more popular than the other types for CO_2 adsorption. For instance, the modification of mesoporous silica gel with choline chloride improved its CO_2 adsorption capacity at 25 °C to 51 mg g^{-1}.[32] In addition, a nano-composite adsorbent functionalised with DES mixture (ChCl–urea)[33] also produced a maximum capacity of 23.0 mg g^{-1} in a comparable work. Zulkurnai *et al.*[21] also investigated and analysed the CO_2 adsorption capacity of choline chloride-based DES. Compared to raw activated carbon, the DES-based activated carbon had a higher CO_2 adsorption removal at 9.851 mg g^{-1}.[21] Chloride–glycerol DES showed a higher CO_2 adsorption capacity (20.1 mg g^{-1}) than choline chloride–ethylene glycol at a capacity of 18.8 mg g^{-1}.[34] In the case of SO_2 removal here, KCC-1/DES1 (utilising choline chloride–glycerol) also shows better performance than fresh KCC-1 and KCC-1/DES2 (with choline chloride–ethylene glycol).

3.2.1 Chemical characterization using FTIR. The FTIR spectra for all three samples before and after SO_2 adsorption are shown in Fig. 3(a) and (b), respectively, while the possible surface functional groups are listed in Table 2. The spectra of blank KCC-1 prior to the adsorption process in Fig. 3(a) show several peaks around 796 cm^{-1}, 1058 cm^{-1} and 1206–1228 cm^{-1}, corresponding to Si–O symmetric, asymmetric, and stretching vibrations, respectively.[35] Upon modification with DES, the transmittance of the peak at 1058 cm^{-1} increases due to the presence of the O–H group, while the increment of the peak around 1206–1228 cm^{-1} can be ascribed to the appearance of a C–O stretching bond.

Additionally, six new peaks appear on the FTIR spectra of the DES-modified KCC-1 samples, corresponding to the presence of various functional groups. A stretching bond can be seen around 3455 cm^{-1}, corresponding to SiO–H associated with silanol, O–H group indicating the presence of water and N–H stretching pertaining to amides and amine groups.[36] The peak around 3016 cm^{-1} can also be attributed to water adsorbed on the surface of the modified KCC-1.[37] The presence of water on the surface of the adsorbent may result in a slower adsorption rate and limit the mass transfer capacity.[38] Water molecules can preferentially compete with SO_2 for adsorption sites if the adsorbent has a higher affinity for water, leaving fewer sites available for the SO_2 molecules.[39] In addition, a slower diffusion rate can limit the overall adsorption capability as the water molecules create a barrier of diffusion, hindering the movement of SO_2 molecules into the pores of the adsorbent.[40] Nonetheless, based on the spectra, the transmittance intensity related to water is significantly lower than the other compounds; therefore, it can be concluded that the effect of water on SO_2 adsorption is minimal.

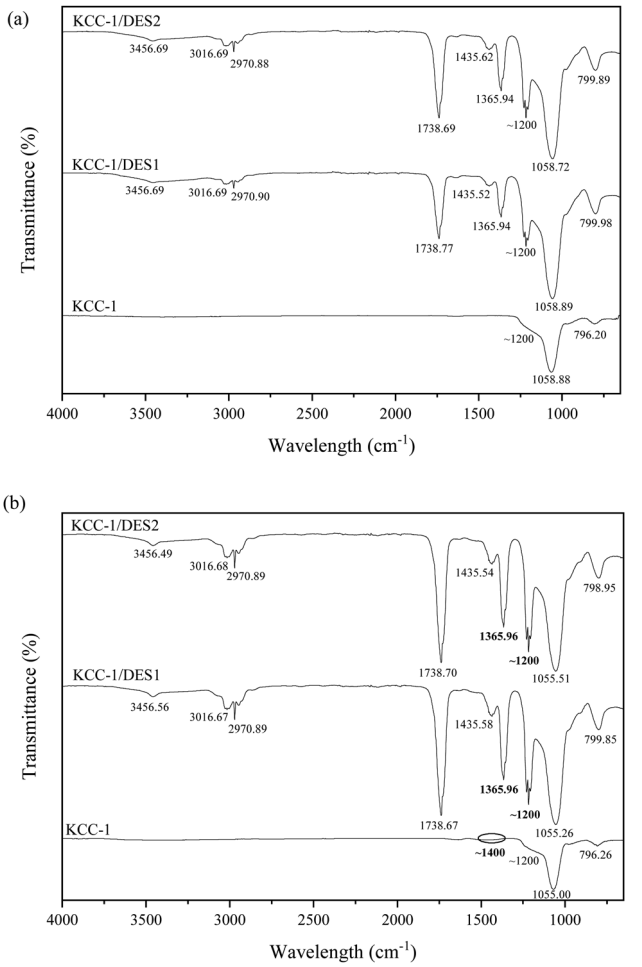

Fig. 3 FTIR spectra of all samples (a) before and (b) after SO_2 adsorption.

On the other hand, the observed N–H stretching proves the presence of choline chloride on the surface of DES-modified KCC-1 samples. The N-element is expected to aid in SO_2 capture and successful bonding to the surface of KCC-1 samples.[21] A sharp, small peak corresponding to C–H symmetric and asymmetric stretching vibrations associated with alkanes and alkenes is detected around 2970 cm^{-1} across all samples.[41]

A significant peak is observed in the FTIR spectra of all DES-modified KCC-1 samples at around 1738 cm^{-1} corresponding to C═O stretching, suggesting the presence of saturated aliphatic compounds from alkane groups probably originating from both HBA and HBD elements of the DES.[22] Meanwhile, due to the chemical nature of HBD component, all samples show C–H bonding in the 1435 cm^{-1} range, possibly ascribed to an alkane group.[42]

The chemical heterogeneity of the sorbent's surface also determines the extent and feasibility of an adsorption mechanism. The presence of heterocyclic compounds containing sulphur (S), nitrogen (N) and oxygen (O) influences the surface chemical heterogeneity. The specific quantity and form of

Table 2 Possible functional groups on the surface of fresh KCC-1 and DES-modified KCC-1 before and after SO_2 adsorption

	Peak wavelength (cm^{-1})					
	KCC-1		KCC-1/DES1		KCC-1/DES2	
Possible functional group	Before	After	Before	After	Before	After
Si–O–H, O–H group, N–H group	—	—	3455.69	3456.56	3456.37	3456.49
O–H group	—	—	3016.69	3016.67	3016.69	3016.68
C–H symmetric and asymmetric stretching vibration	—	—	2970.90	2970.89	2970.88	2970.89
–COOH group	—	—	1738.77	1738.67	1738.69	1738.70
C–H bending vibration	—	—	1435.62	1435.58	1435.52	1435.54
SO_2	—	~1200, ~1400	—	~1200, ~1360	—	~1200, ~1360
O–H group	—	—	1365.94	1365.96	1365.94	1365.96
Si–O stretching vibration, C–O stretching vibration	1228.86, 1217.09, 1206.16	1228.86, 1217.11, 1206.16	1228.41, 1217.05, 1205.98	1228.77, 1217.10, 1206.04	1228.64, 1217.07, 1205.79	1228.76, 1217.10, 1206.01
Si–O asymmetric vibration, O–H group	1058.85	1055.00	1058.89	1055.26	1058.72	1055.51
Si–O symmetric vibration	796.20	796.26	799.98	799.85	799.89	798.95

heteroatoms depend on the modification methods and materials from which the atoms are derived. The presence of basic groups with strong affinity improves interaction; however, this is not the point at which adsorption becomes entirely chemisorption.[43] On the other hand, an acidic character is caused by oxygen-containing functionalities that form during oxidation synthesis, giving the sorbents electron-acceptor properties. In contrast, N-containing functionalities are typically basic in nature. These functionalities also have electron-donor properties, making them attractive sites for the electron-deficient S-atom in SO_2.[44] At low temperatures, imines, amines, amides, imides, and nitriles will predominate in specific N-functionalities produced during modification. Although both O- and N-surface functional groups can improve SO_2 adsorption, the presence of O prior to N-doping can further enhance the effectiveness of N-functionalisation significantly.[45]

Oxygen-containing groups influence two key properties of sorbents: their hydrophilicity or hydrophobicity, and their basicity or acidity. The number of polar O-groups influences the degree of hydrophilicity. Carbon oxidation introduces various O-functionalities and endows the surface with electron-acceptor properties. For instance, lactone and phenol groups contribute to surface acidity, whereas surface basicity is caused by pyrone, carbonyl, benzopyran and alcohol groups.[46,47] Nitrogen surface functional groups are not the only species with basic properties; other O-containing groups with basic properties include alcohols, carbonyls, and ethers, which contain electron-donating O-atoms capable of having electrostatic interactions with SO_2, thereby enhancing adsorption.[48,49] The framework whereby SO_2 is adsorbed due to these functional groups can be evaluated by classifying them according to their intrinsic heteroatoms. These functional groups are as complicated as the techniques utilised to introduce them. It is difficult to assume that these groups are entirely independent of one another, and further research is still required to clarify any potential antagonistic effects among these groups in the context of SO_2 adsorption.[45]

Based on the literature, peaks related to SO_2 can be observed in typical FTIR spectra around 1150–1210 cm^{-1} and 1340–1400 cm^{-1} corresponding to the symmetric and asymmetric vibrations of SO_2 molecules, respectively.[50–52] In this work, a tiny peak can be observed in Fig. 3(b) around 1400 cm^{-1} on the unmodified KCC-1 spectra, while a significantly enhanced peak can be seen around 1365 cm^{-1}, corresponding to the asymmetric vibration of adsorbed SO_2 molecules in both DES-modified samples. The presence of these new vibrational peaks may result from the formation of a charge-transfer complex due to the interactions between SO_2 molecules and lone pair of electrons on N (N:), leading to the formation of an antibonding SO_2 orbital (N → SO_2).[52] On the other hand, the presence of symmetric SO_2 molecules is more difficult to determine, as the peak could have merged with the adjacent peaks around 1200 cm^{-1}, corresponding to Si–O and C–O stretching vibrations. Nonetheless, the sharp increment of the transmittance intensity at this frequency strongly suggests the presence of symmetric SO_2 on the adsorbent. This is an indication that SO_2 molecules are adsorbed on active sites comprising silica-based radicals ($\equiv$Si–O$^{\bullet}$ and $\equiv$Si$^{\bullet}$) on KCC-1, similar to that suggested by literature.[53] The minimal change in FTIR spectra of the unmodified KCC-1 in comparison to the DES-modified samples after SO_2 adsorption demonstrates the importance of DES in the process as the interaction between SO_2 molecules and unmodified KCC-1 is very weak[52]

3.2.2 Physical characterization using FESEM and BET. The FESEM micrographs for KCC-1, KCC-1/DES1, and KCC-1/DES2 are shown in Fig. 4(a)–(c). It can be observed in Fig. 4(a) that the KCC-1 spheres have average diameters of approximately 275.6–287.5 nm, which are similar to values reported by previous studies.[11,20] However, the diameters increase to 288.4–305.1 nm and 295.9–307.5 nm for DES-modified samples, KCC-1/DES1 and KCC-1/DES2, respectively.

In each figure, the colloidal nanospheres reveal well-defined fibrous structures made of three-dimensional arrangements of dendrimeric fibres. Because of the existence of these dendrimeric fibres, the available high surface area of fresh and modified KCC-1 samples may become easily accessible.[10] As analysed in Section 3.1, KCC-1/DES1 (with choline chloride) has the highest adsorption capacity of 191.88 mg g^{-1}, surpassing the other samples. On the other hand, KCC-1/DES2 modified with ethylene glycol has

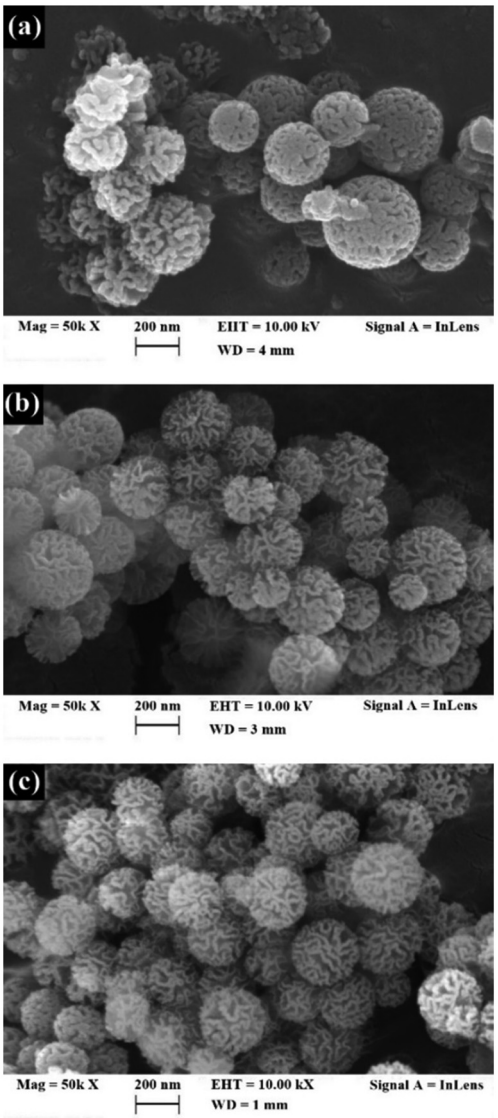

Fig. 4 FESEM micrographs for (a) KCC-1, (b) KCC-1/DES1 and (c) KCC-1/DES2.

lower adsorption capacity despite having the largest size (average diameter of 301.70 nm), as shown in Fig. 4(b), indicating that the larger the diameter of the nanospheres, the lower the saturation surface concentration. This is because larger particle sizes have less curvature, lower deviation from a flat surface, fewer number of active site densities, and thus less surface adsorbates.[54] In addition, unmodified KCC-1 has the smallest sphere diameter with an average of 281.55 nm; however, the adsorption capacity is also lower by 3.92 times than the modified KCC-1/DES1. This indicates that the nature of interaction between unmodified KCC-1 and SO_2 is weak, and there is a shortage of active sites.[55]

The surface properties of nanospheres are size-dependent, with smaller particles having a higher affinity to adsorb SO_2 and decontaminating more slowly, as evidenced by a longer saturation time. A possible explanation of the increase in KCC-1 particle size upon DES modification, is that the high concentration of the modified sample allows a faster rate of precursor hydrolysis. This rapid hydrolysis contributes more to particle size growth than nucleation rate, causing mesoporous silica particle to increase in size with higher concentration; one of the major variables influencing particle size.[56] Furthermore, the catalyst molar ratio also contributed to the increase in the particle size of the mesosphere.[57]

N_2 adsorption–desorption isotherm of KCC-1 and modified KCC-1 samples are shown in Fig. 5, while the properties of the samples (surface area, total pore volume and average pore size) are summarized in Table 3.

The isotherm plots are offset along the *y*-axis for better comparison among the samples. The N_2 adsorption–desorption isotherm of KCC-1 and DES-modified KCC-1 shown in Fig. 5 can be classified as type IV(a) isotherm with H3 hysteresis loop in P/P_0 range of 0.4–1.0. This implies that the pores of all samples demonstrate mesoporous properties with characteristics of capillary condensation and non-uniform slit-shaped pores.[58] The N_2 uptake by the samples follows the order of KCC-1 > KCC-1/DES1 > KCC-1/DES2, where slight reduction demonstrated by the DES-modified KCC-1 can be attributed to blockage of interparticle pores due to the introduction of DES onto the KCC-1 surface.[59] As shown in Table 3, the surface area and total pore volume of KCC-1 samples slightly decrease upon modification with DES, possibly due to the dispersion of DES,

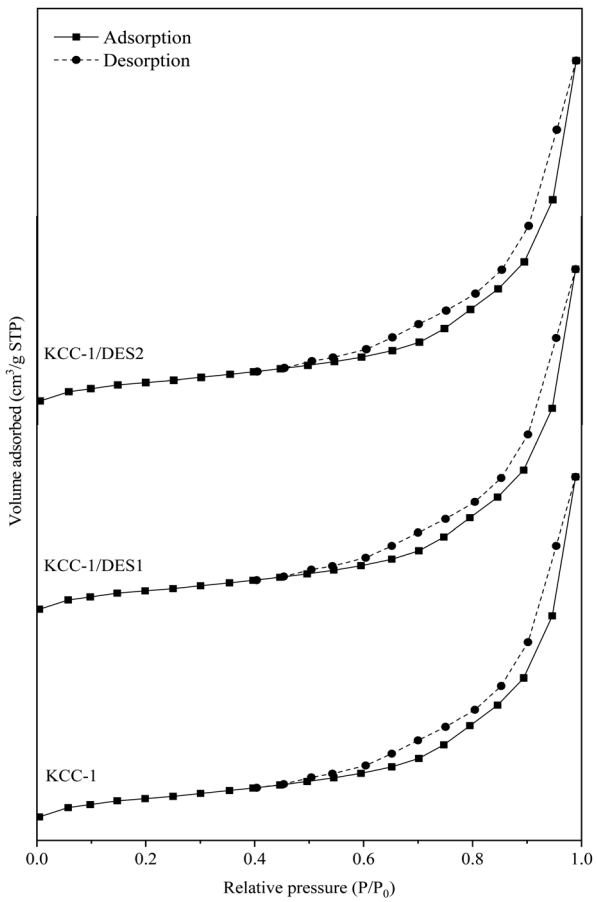

Fig. 5 N_2 adsorption–desorption isotherms for KCC-1 and DES-modified KCC-1.

Table 3 SO_2 removal performance of KCC-1 and DES-modified KCC-1 samples

Sample	Surface area (m^2 g^{-1})	Total pore volume (cm^3 g^{-1})	Average pore size (nm)
KCC-1	553.07	0.1170	2.186
KCC-1/DES1	528.78	0.1138	2.208
KCC-1/DES2	524.43	0.1123	2.201

which partially blocks the available pores, as mentioned earlier. On the other hand, the average pore size of KCC-1 samples shows a minor increment with the presence of DES, possibly due to partial breakage of the silica framework, which may also contribute to the reduced surface area.[60]

3.3 Effects of different inlet concentrations

The effect of inlet SO_2 concentration was investigated using KCC-1/DES1 (chosen based on the breakthrough study in Section 3.1) at various concentrations ranging from 1500 to 2000 ppm, reflecting typical SO_2 concentrations released by medium to high sulphur-content fossil fuels.[61] Fig. 6 shows the breakthrough curves of SO_2 adsorption at varying SO_2 concentrations, while Table 4 summarizes breakthrough time, MTZ and adsorption capacity at different inlet SO_2 concentrations. As the SO_2 concentration is already relatively high at 1500 ppm, further increase to 2000 ppm with the same amount of adsorbent decreases the adsorption capacity of KCC-1/DES1 from 4.84 to 2.73 mg g^{-1}. The decrease in SO_2 adsorption capacity with an increase in SO_2 concentration or the uptake of SO_2 molecules supplied per g of adsorbent could be attributed to the higher number of SO_2 molecules available, which may remain unabsorbed at a constant adsorbent mass. This results in quick occupancy of the available active sites, which subsequently causes rapid breakthrough and saturation of the adsorbent bed.

A higher SO_2 concentration also results in a greater driving force due to the steeper concentration gradient between SO_2 in the gas phase and on the adsorbent's surface. This gradient acts as a driving force for diffusion, causing SO_2 molecules to move from the gas phase towards the adsorbent,[62] inducing an effect similar to the influence of a high SO_2 flow rate on MTZ, as mentioned in Section 3.2. The limitation in the capacity of the adsorbent bed as the SO_2 concentrations increase has also been reported by others.[24,63] However, a fixed-bed desulphurisation efficiency is also influenced by numerous other factors such as the preparation method, activity, the type of desulphurising agent, SO_2 concentration, pressure and bed temperature. Based on the results, it can be concluded that an optimum capacity for SO_2 removal could be attained under lower concentration conditions, emphasising the crucial role that concentration plays for effective adsorption.[64]

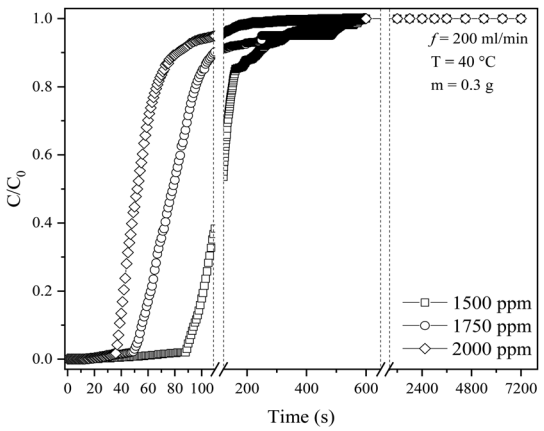

Fig. 6 SO_2 breakthrough curves of KCC-1/DES1 at different SO_2 concentrations.

Table 4 SO_2 removal performance of KCC-1/DES1 at different SO_2 concentrations

Inlet concentration (ppm)	Breakthrough time at C/C_0 = 0.05 (s)	Time at C/C_0 = 0.95 (s)	MTZ (%)	Adsorption capacity at C/C_0 = 0.95 (mg SO_2 per g sample)
1500	91	332	92.17	4.84
1750	53	250	90.80	3.49
2000	38	105	83.81	2.73

3.3.1 Isothermal studies. Nonlinear methods were employed to fit the experimental data to the Langmuir, Freundlich and Toth adsorption isotherms. Fig. 7(a)–(c) show the isotherm plots, while Table 5 summarises the calculated model parameters. The results indicate that the experimental data are better correlated to Toth and Langmuir isotherms than to the Freundlich isotherm. Between the former two models, Toth isotherm shows a better fit based on its correlation coefficient (R^2) values exceeding 0.965 for all studied SO_2 inlet concentrations (1500, 1750, 2000 ppm). In addition, the maximum adsorption capacity (q_m) obtained from the Toth model and the adsorption capacity achieved experimentally show similar trends and magnitudes.

All samples fit well with the Toth isotherm, with N_T values less than 1, which indicates localized multilayer adsorption of interacting particles onto heterogeneous surface systems.[65] The N_T parameter quantifies the adsorption system's heterogeneity, and a deviation from unity suggests that the system is heterogeneous.[66] On the other hand, the Toth equation simplifies to the Langmuir isotherm when N_T = 1. A study by Avijegon *et al.*[67] also concluded that the adsorption of natural gas may be well characterized by a Toth isotherm model, with parameters derived from data regression for CO_2, CH_4, and N_2 mixtures within the same pressure and temperature ranges, along with the experimental binary and ternary adsorption equilibrium data.[67]

Based on Table 5, a fascinating trend can be observed concerning the role of SO_2 concentration in the adsorption process, *i.e.* N_T decreases with increasing SO_2 concentration (0.92 at 1500 ppm, 0.53 at 1750 ppm, and 0.62 at 2000 ppm). As mentioned earlier, an N_T value closer to 1 at a lower SO_2 concentration signifies a relatively uniform surface, consistent with the Langmuir model. However, the subsequent decrease in N_T values with increasing SO_2 concentrations suggests a shift towards a more heterogeneous surface. This trend indicates

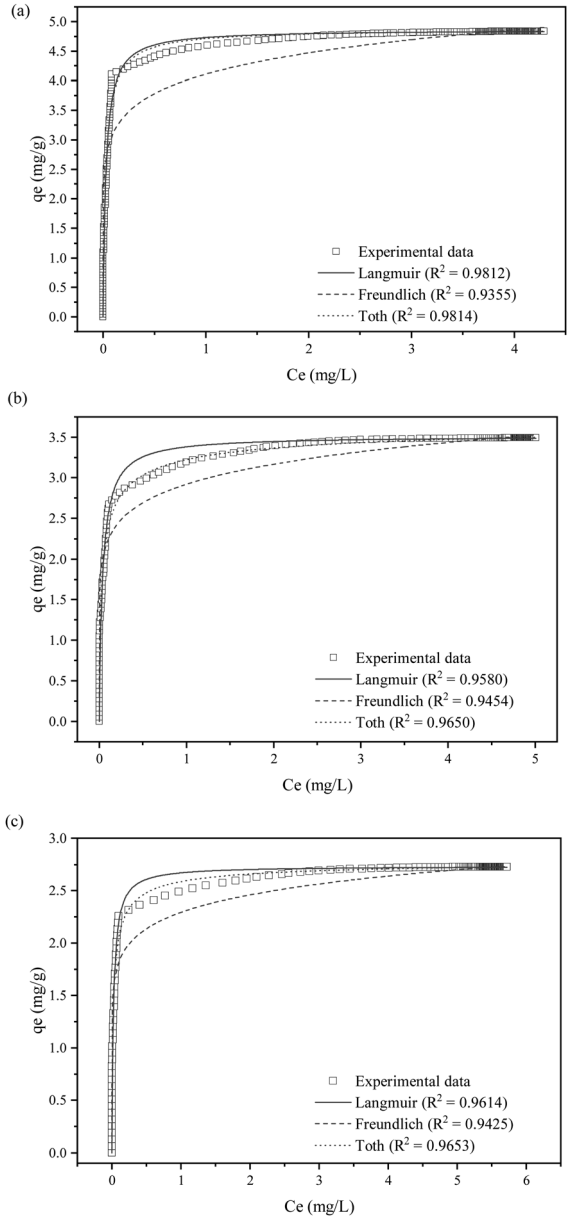

Fig. 7 Nonlinear fittings of SO_2 removal at (a) 1500 ppm, (b) 1750 ppm and (c) 2000 ppm SO_2 initial concentrations with Langmuir, Freundlich and Toth isotherm model.

that the higher SO_2 concentrations may be altering the surface properties of the adsorbent as the SO_2 molecules preferentially occupy the most favourable sites at lower concentrations, leaving a wider distribution of lower-energy sites that contribute to adsorption at higher concentrations.

Furthermore, the interaction of KCC-1/DES1 with SO_2 may modify its surface chemistry, creating new adsorption sites with varied energies. The observed decreasing trend in N_T values of Toth isotherm provides compelling evidence that high SO_2 concentrations lead to a more heterogeneous surface, resulting in non-uniform adsorption behaviour. Similar interaction patterns between adsorption behaviour and SO_2 concentration are also observed in other studies.[68–71]

Table 5 Parameters of three isotherm models fitted with adsorption data at different reaction concentrations

	SO_2 concentration (ppm)		
Isotherm model	1500	1750	2000
Langmuir			
R^2	0.9812	0.9580	0.9614
K_L	35.424	25.320	41.089
q_m	4.8635	3.5148	2.7359
Freundlich			
R^2	0.9355	0.9454	0.9650
K_F	4.1103	2.9195	2.2928
Toth			
R^2	0.9814	0.9650	0.9653
K_T	40.409	115.84	117.64
N_T	0.9208	0.5301	0.6217
q_m	4.8801	3.7305	2.8049

3.4 Effects of different reaction temperatures

SO_2 adsorption was studied at various temperatures for kinetic investigation, and the resulting breakthrough curves are presented in Fig. 8. The MTZ and adsorption capacity at all studied temperatures are summarized in Table 6. The SO_2 adsorption capacity is observed to decrease by 2.51 and 2.80 times with an increase in the reaction temperature from 40 °C to 80 and 120 °C, respectively. This is expected as increased temperatures generally inhibit gas adsorption; therefore, the greater the temperature, the lower the gas adsorption capacity, whereas elevated pressures promote adsorption.[72] As the temperature increases from 40 to 120 °C, the percentage of MTZ also decreases after a contact period of 91, 36 and 29 s under the three different temperatures, respectively, indicating that the adsorption process is optimum at lower temperatures. Similar findings was reported by Delgado *et al.*,[63] who observed that the rise in temperature from 298 K to 308 K decreased the breakthrough time and adsorption capacity by 21.6% and 23.6%, respectively.

At higher temperatures, the breakthrough time and total adsorption rate decrease faster than the growth rate. As a result,

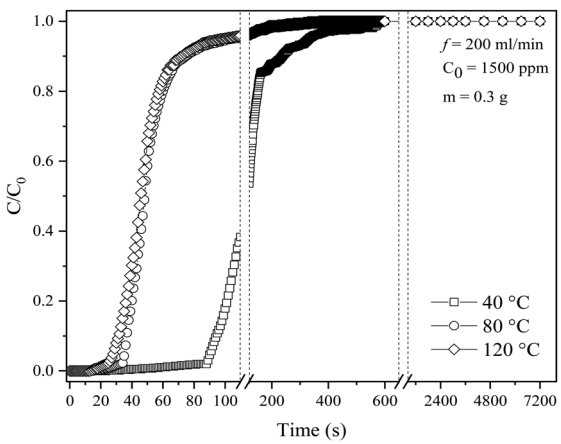

Fig. 8 SO_2 breakthrough curves of KCC-1/DES1 at different temperatures.

Table 6 SO_2 removal performance of KCC-1/DES1 at different temperatures

Temperature (°C)	Breakthrough time at C/C_0 = 0.05 (s)	Time at C/C_0 = 0.95 (s)	MTZ (%)	Adsorption capacity at C/C_0 = 0.95 (mg SO_2 per g sample)
40	91	332	92.17	4.84
80	36	106	83.02	1.93
120	29	87	76.00	1.73

the adsorption capacity and breakthrough time decrease by 34.3% and 27.8%, respectively, as the temperature rises from 40 °C to 120 °C. It can be inferred that the temperature increase has a negative impact on the adsorption performance,[63] influenced by two main factors: the exothermic nature of the adsorption process and kinetic effects. As the temperature increases, the system becomes less favourable for the adsorption reaction. The adsorbate molecules (SO_2) have additional thermal energy, making them less likely to adhere to the adsorbent surface and increasing their tendency to desorb into the gas phase. Moreover, the adsorbate molecules have higher kinetic energy at high temperatures, leading to more frequent collisions with the surface, making it harder to achieve successful adsorption as they may collide and bounce off the surface instead of forming stable interactions.[73,74]

3.4.1 Kinetic studies. As mentioned earlier, to study the kinetic parameters, the breakthrough experimental data was plotted using non-linearised kinetic models: P1st, P2nd and Avrami. The nonlinear P1st, P2nd and Avrami kinetic plots of SO_2 adsorption on KCC-1/DES1 at temperatures of 40, 80 and 120 °C are shown in Fig. 9(a)–(c), respectively, while Table 7 summarises the estimated parameters and R^2 values.

The adsorption rate for P1st, K_1, increases from 1.040 to 2.930 with the temperature increase. A similar rise in adsorption rate is also recorded for P2nd's K_2 and Avrami's K_3. The nonlinear Avrami kinetic plots show R^2 values above 0.99 across all tested temperatures, higher than P1st (above 0.96) and P2nd (between 0.85 and 0.88), indicating that the experimental data fit better to the Avrami model. The Avrami model assumes that adsorption happens through both chemisorption and physisorption pathways. Avrami exponents (N_A) that range from 1.576 to 1.642 indicate a one-dimensional growth of adsorbed SO_2 molecules on the accessible active sites of the KCC-1/DES1 surface. In SO_2 adsorption mechanisms, $N_A > 1$ also implies the coexistence of physisorption and chemisorption.[69]

Previous studies on gas adsorption, including CO_2, NO and H_2S have demonstrated the suitability of explaining the adsorption kinetics using Avrami kinetic model.[75–79] However, the validity of this model in SO_2 adsorption study is limited. In addition, SO_2 adsorption is mutually reported by various studies as exothermic, implying that the process is negatively governed by the reaction temperature.[20]

The P1st kinetic model is generally suitable to describe purely physical adsorption processes characterised by low surface coverage and fairly describe the reversible interactions between the adsorbate and adsorbent surfaces, without accounting for chemical bonding or interactions[80] between

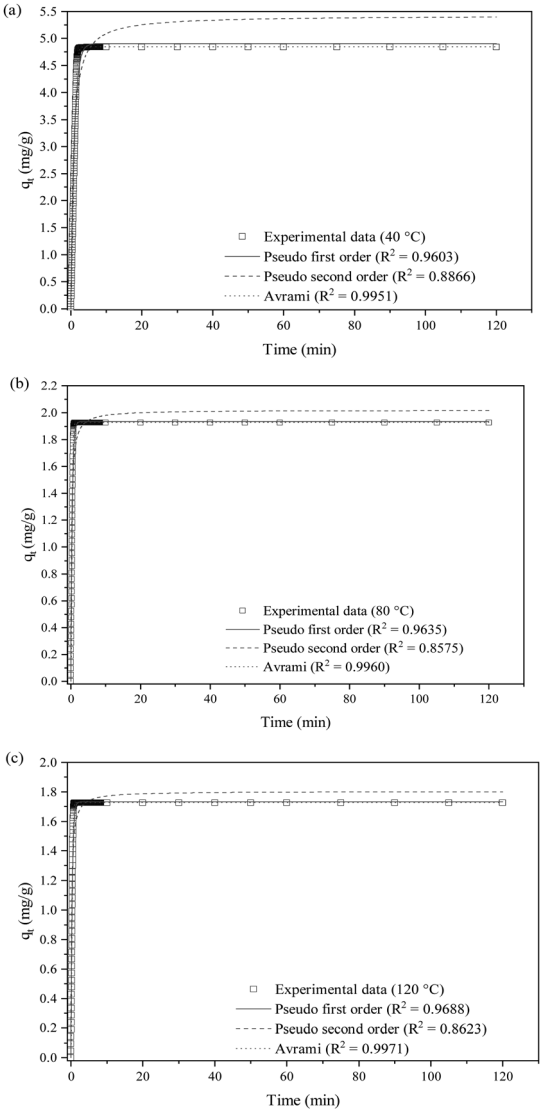

Fig. 9 Non-linear fittings of SO_2 removal at (a) 40 °C, (b) 80 °C and (c) 120 °C with P1st, P2nd and Avrami kinetic models.

Table 7 Parameters of three kinetic models fitted with adsorption data at different reaction temperatures

	Kinetic model						
	Pseudo-first-order (P1st)		Pseudo-second-order (P2nd)			Avrami	
Temperature (°C)	R^2	K_1	R^2	K_2	R^2	K_3	N_A
40	0.961	1.040	0.887	0.278	0.995	0.986	1.642
80	0.963	2.681	0.857	2.484	0.996	2.486	1.640
120	0.969	2.930	0.862	3.105	0.997	2.728	1.576

SO_2 molecules and the surface of KCC-1/DES1. The model's fit improves as the adsorption temperature increases and the surface coverage is reduced due to the thermodynamic limitations associated with the exothermicity of the adsorption process. On the other hand, Fig. 9(a)–(c) and Table 7 reveal

that the P2nd model does not fit well with the experimental data compared to the P1st model. As the P2nd kinetic model is more suitable to describe chemisorption processes induced by strong chemical bonds between molecules and the sorbent surface rather than a process with simultaneous occurrence of physisorption and chemisorption,[81] the model is not examined further for SO_2 adsorption on KCC-1/DES1.

Meanwhile, the Avrami model fits well with the experimental data across all studied temperatures. The excellent fit is believed to be due to its capacity to account for both physical and chemical adsorption mechanisms.[82] Since the SO_2 adsorption mechanism on KCC-1/DES1 is neither purely chemisorption nor physisorption, the SO_2 uptake may originate from two different pathways.[80] Initially, SO_2 molecules may adsorb onto the surface through weak van der Waals interactions (physisorption). As the surface coverage increases, some of these molecules may undergo a transition to chemisorption, forming stronger chemical bonds with the surface.[80,83] This hybrid adsorption mechanism is further supported by the comparable fit of the adsorption data to both P1st ($R^2 \approx 0.96$) and Avrami ($R^2 \approx 0.99$) kinetic models, suggesting contributions from both physical and chemical interactions. In addition, the kinetic constants (k_1, k_2 and k_3) reported in Table 7 show that the kinetic parameters increase with temperatures, indicating that the adsorption rate is favoured at higher temperatures. However, the adsorption rate becomes faster (lower amount of SO_2 is adsorbed on KCC-1/DES1; lower adsorption capacity) at high temperatures, as tabulated in Table 6. Therefore, the adsorption of SO_2 onto KCC-1/DES1 is characterized by a kinetic-thermodynamic trade-off. At higher temperatures, the adsorption rate increases due to kinetic factors, but the thermodynamically unfavourable exothermic process limits the overall adsorption capacity.

Moreover, the N_A values shown in Table 7 are always larger than 1, suggesting that SO_2 adsorption is not homogeneous (not adsorbed with the same probability over different regions of the sorbent surface).[84,85] These results are consistent with the findings reported in previous thermodynamic study,[20] confirming that SO_2 adsorption on KCC-1 is heterogeneous. Most likely, the initial occupation of adsorption sites is uniform; however, as the adsorption proceeds, additional adsorption preferentially occurs near existing adsorption sites, resulting in deviations from the uniformity of adsorption sites and a value of N_A greater than 1.[86,87] More specifically, N_A is always around 1.6, indicating that the adsorption rate decreases gradually with the one-dimensional growth of the adsorbed nuclei, and the little variations of N_A with increasing temperatures suggest that the underlying adsorption mechanism does not change.

3.4.2 Thermodynamic study. The SO_2 adsorption isotherm data at various reaction temperatures ranging from 40 to 120 °C were used to calculate the adsorption thermodynamics parameters. Fig. 10 plots the thermodynamic equilibrium constant (K_e°) *versus* temperature (T), while Table 8 lists the adsorption thermodynamics parameters. The adsorption process can be assumed spontaneous based on the negative Gibbs free energy

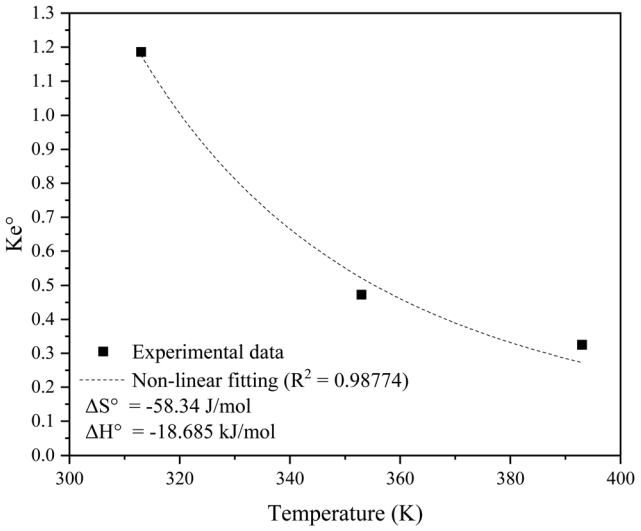

Fig. 10 Non-linear Van't Hoff plot of SO_2 adsorption onto KCC-1/DES1.

(ΔG°), indicating a favourable interaction between SO_2 and the KCC-1/DES1 adsorbent.[88] The ΔH° value for KCC-1/DES1 adsorbent is -18.685 kJ mol^{-1}, which aligns with values reported in other SO_2 adsorption studies using siliceous-based materials (-4.59 to -20.2 kJ mol^{-1}).[89,90] The ΔH° value suggests that physisorption is the primary adsorption mechanism as physical adsorption has been defined in literature as having an activation energy of less than 40 kJ mol^{-1}.[91,92] However, since findings from the kinetic and isotherm studies have indicated that the SO_2 removal process may occur through both physical and chemical adsorptions, it may be safe to assume that SO_2 removal occurs through both pathways, but the physical route predominates.

In general, adsorption of molecules on an adsorbent surface minimises the degree of irregularity. The stronger contact between adsorbed SO_2 molecules and the adsorbent surface compared to interactions with free SO_2 molecules may be responsible for the observed negative ΔH° value. The adsorption process is exothermic, as evidenced by the negative ΔH° value, while the low ΔH° absolute value indicates a weak connection between the adsorbent and adsorbate, characteristic of physisorption. The negative entropy change (ΔS°) suggests that the adsorption process is becoming more ordered with temperature.[93]

The calculated Gibbs free energy (ΔG°) for SO_2 adsorption on KCC-1 at different temperatures range between -0.4224 and 4.2454 kJ. The adsorption process at 40 °C can be assumed spontaneous based on the negative ΔG° value.[88] However, the process becomes non-spontaneous with an increase in temperature to 80 °C and 120 °C as evidenced by the shift to positive ΔG° values. The sorption process is driven by both entropy and enthalpy, according to the values of ΔG°, ΔH°, and ΔS°.[94] The term enthalpy-driven process refers to a process in which the system achieves a more stable state through releasing heat energy. Entropy-driven processes, in addition, indicate that the system evolves in such a way that the arrangement of molecules becomes more random or chaotic. The comparison

Table 8 Thermodynamic parameters of SO_2 removal by KCC-1/DES1

Temperature (°C)	Temperature (K)	ΔS° (J mol^{-1} K^{-1})	ΔH° (kJ mol^{-1})	ΔG° (kJ)
40	313			−0.4224
80	353	−58.347	−18.685	1.9115
120	393			4.2454

of the absolute values of ΔH° and ΔS° serves as the selection indicator. It should be noted that the value of ΔG° increases when the temperature rises, implying that the adsorption process is more feasible at lower temperatures.[95]

4. Conclusions

The possibility of using modified fibrous mesoporous silica, KCC-1, as an alternative sorbent for dry removal of SO_2 is evidenced in this study. The modified sorbent is shown to outperform the unmodified KCC-1 due to a shortage of accessible active sites and the weak interaction between KCC-1 and SO_2. KCC-1 was impregnated with deep eutectic solvents (DES) to compensate for this weakness. The presence of DES1 (choline chloride and glycerol) produces a higher number of accessible active sites, resulting in 3.91 times higher SO_2 removal capacity over unmodified KCC-1 and 4.97 times over KCC-1 modified with DES2 (choline chloride and ethylene glycol). Choline chloride and glycerol based DES impregnation results in more significant mesoporosity growth and higher SO_2 adsorption capability. The Avrami kinetic model, which assumes numerous physisorption and chemisorption pathways, best represent SO_2 adsorption on optimised KCC-1/DES1 across all studied reaction temperatures. The adsorption process progresses from a random stage on the surface of KCC-1 to a more ordered stage with higher degrees of freedom as the adsorbed SO_2 becomes more dispersed. Based on the Gibbs free energy, the process is spontaneous and highly favourable at lower reaction temperatures. The experimental data at varying inlet SO_2 concentrations are consistent with the Toth isotherm model, indicating the presence of localised multilayer adsorption onto a heterogeneous surface. Overall, these findings suggest that SO_2 adsorption is favoured at lower reaction temperatures and incoming SO_2 concentrations, due to the exothermic nature of the process and the slower sorbent saturation.

Data availability

All data generated or analysed during this study are included in this article. Raw data are available upon request.

Conflicts of interest

There are no conflicts to declare.

Acknowledgements

The authors would like to acknowledge the support from the Faculty of Civil Engineering & Technology, Universiti Malaysia Perlis and Universiti Teknologi Malaysia for providing the mesoporous silica KCC-1.

References

1 World Health Organization, Ambient (outdoor) air pollution, 2022.
2 U.S. Centers For Disease Control and Prevention, Carbon Monoxide Poisoning, 2024.
3 United States Environmental Protection Agency, Particulate Matter (PM) Pollution, 2024.
4 United States Environmental Protection Agency, Sulfur Dioxide (SO2) Pollution, 2024.
5 K. Naderi, M. S. Kalami Yazdi, H. Jafarabadi, F. Bahmanzadegan, A. Ghaemi and M. R. Mosavi, *Sci. Rep.*, 2024, **14**, 954.
6 United States Environmental Protection Agency, Air pollution control technology fact sheet, 2022.
7 A. Upadhyay, *Electrical India*, 2020.
8 M. A. Hanif, N. Ibrahim and A. Abdul Jalil, *Environ. Sci. Pollut. Res.*, 2020, **27**, 27515–27540.
9 X. Li, L. Zhang, Y. Zheng and C. Zheng, *Energy Fuels*, 2015, **29**, 942–953.
10 V. Polshettiwar, D. Cha, X. Zhang and J. M. Basset, *Angew. Chem., Int. Ed.*, 2010, **49**, 9652–9656.
11 N. Bayal, B. Singh, R. Singh and V. Polshettiwar, *Sci. Rep.*, 2016, **6**, 24888.
12 R. Soltani, A. Marjani, M. Hosseini and S. Shirazian, *Chemosphere*, 2020, **239**, 124735.
13 S. Sun, Y. Niu, Q. Xu, Z. Sun and X. Wei, *Ind. Eng. Chem. Res.*, 2015, **54**, 8019–8024.
14 F. Zarei, A. Marjani and R. Soltani, *Eur. Polym. J.*, 2019, **119**, 400–409.
15 K. Yu, X. Zhang, H. Tong, X. Yan and S. Liu, *Mater. Lett.*, 2013, **106**, 151–154.
16 H. S. Oboudatian and J. Safaei-Ghomi, *Sci. Rep.*, 2022, **12**, 2381.
17 L. W. Lai, L. P. Teh, S. N. Timmiati, N. H. N. Kamarudin and H. D. Setiabudi, *J. Environ. Chem. Eng.*, 2023, **11**, 111295.
18 M. B. Singh, V. S. Kumar, M. Chaudhary and P. Singh, *J. Indian Chem. Soc.*, 2021, **98**, 100210.
19 D. Yang, S. Zhang, D. Jiang and S. Dai, *Phys. Chem. Chem. Phys.*, 2018, **20**, 15168–15173.
20 M. A. Hanif, N. Ibrahim, K. Md Isa, F. Muhammad Ridwan, T. A. Tuan Abdullah and A. A. Jalil, *Microporous Mesoporous Mater.*, 2022, **330**, 111610.
21 N. Z. Zulkurnai, U. F. Md Ali, N. Ibrahim and N. S. Abdul Manan, *IOP Conf. Ser.: Mater. Sci. Eng.*, 2017, **206**, 012001.
22 C. Y. Lim, M. F. Majid, S. Rajasuriyan, H. F. Mohd Zaid, K. Jumbri and F. K. Chong, *Environments*, 2020, **7**, 97.
23 S. H. Ammar and S. A. Jaffar, *Eng. Technol. J.*, 2017, **35**, 856–863.

24 M. A. Hanif, N. Ibrahim, K. Md. Isa, U. F. Md. Ali, T. A. Tuan Abdullah and A. A. Jalil, *J. Porous Mater.*, 2022, **29**, 501–514.
25 R. Guo, S. Li, L. Zhao, Y. Zhao, W. Lu, P. Yuan, P. Deng and F. Liao, *J. Zhejiang Univ., Sci., B*, 2007, **8**, 867–874.
26 T. R. Sahoo and B. Prelot, *Nanomaterials for the Detection and Removal of Wastewater Pollutants*, Elsevier, 2020, pp. 161–222.
27 R. Chang and J. W. J. Thoman, *Physical Chemistry for the Chemical Sciences*, Universiti Science Books, 2014.
28 R. Manurung, G. C. Simanjuntak, R. N. Perez, A. Syahputra, M. A. Alhamdi, H. Siregar and R. R. Syahputri Zuhri, *IOP Conf. Ser.: Mater. Sci. Eng.*, 2019, **505**, 012134.
29 H. Qin, X. Hu, J. Wang, H. Cheng, L. Chen and Z. Qi, *Green Energy Environ.*, 2020, **5**, 8–21.
30 P. Makoś, E. Słupek and J. Gębicki, *Microchem. J.*, 2020, **152**, 104384.
31 D. T. Mekonnen, E. Alemayehu and B. Lennartz, *Materials*, 2021, **14**, 5466.
32 Z. Ghazali, N. Suhaili, M. N. A. Tahari, M. A. Yarmo, N. H. Hassan and R. Othaman, *J. Mater. Res. Technol.*, 2020, **9**, 3249–3260.
33 Z. Ghazali, M. A. Yarmo, N. H. Hassan, L. P. Teh and R. Othaman, *Arab. J. Sci. Eng.*, 2020, **45**, 4621–4634.
34 Z. Ghazali, M. A. Yarmo and R. Othaman, *AIP Conf. Proc.*, 2019, **2111**, 050014.
35 R. Soltani, R. Pelalak, M. Pishnamazi, A. Marjani, A. B. Albadarin, S. M. Sarkar and S. Shirazian, *Sci. Rep.*, 2021, **11**, 2716.
36 J. Luo, O. Conrad and I. F. J. Vankelecom, *J. Mater. Chem.*, 2012, **22**, 20574.
37 G. Kaur, N. Singh, A. Rajor and J. P. Kushwaha, *J. Contam. Hydrol.*, 2021, **242**, 103847.
38 C. K. Rojas-Mayorga, I. A. Aguayo-Villarreal, J. Moreno-Pérez, R. Muñiz-Valencia, M. Á. Montes-Morán and R. Ocampo-Pérez, *J. Environ. Chem. Eng.*, 2021, **9**, 104810.
39 X. Yang, Q. Wang, J. Chen, H. Liu, L. Xu and M. Rao, *Processes*, 2024, **12**, 1547.
40 Y. Sabahi, M. Razmkhah and F. Moosavi, *Results Chem.*, 2022, **4**, 100283.
41 R. K. Ibrahim, A. El-Shafie, L. S. Hin, N. S. B. Mohd, M. M. Aljumaily, S. Ibraim and M. A. AlSaadi, *J. Environ. Manage.*, 2019, **235**, 521–534.
42 B. H. Stuart, *Infrared Spectroscopy: Fundamentals and Applications*, John Wiley & Sons Ltd, 2004.
43 Y.-C. Chiang and R.-S. Juang, *J. Taiwan Inst. Chem. Eng.*, 2017, **71**, 214–234.
44 A. A. Adelodun, K.-H. Kim, J. C. Ngila and J. Szulejko, *Appl. Energy*, 2015, **158**, 631–642.
45 B. Petrovic, M. Gorbounov and S. Masoudi Soltani, *Carbon Capture Sci. Technol.*, 2022, **3**, 100045.
46 C. Goel, H. Bhunia and P. K. Bajpai, *RSC Adv.*, 2015, **5**, 93563–93578.
47 D. Saha and M. J. Kienbaum, *Microporous Mesoporous Mater.*, 2019, **287**, 29–55.
48 M. G. Plaza, K. J. Thurecht, C. Pevida, F. Rubiera, J. J. Pis, C. E. Snape and T. C. Drage, *Fuel Process. Technol.*, 2013, **110**, 53–60.
49 Y. Liu and J. Wilcox, *Environ. Sci. Technol.*, 2013, **47**, 95–101.
50 M. G. Rabbani, R. K. Sasse, S. Behera, P. Jena, J. Liu, P. K. Thallapally, T. Islamoglu, M. K. Shehab, M. M. Kaid, O. K. Farha and H. M. El-Kaderi, *Langmuir*, 2024, **40**, 8024–8034.
51 M. McAnally, J. Bocková, A. Herath, A. M. Turner, C. Meinert and R. I. Kaiser, *Nat. Commun.*, 2024, **15**, 4409.
52 E. Martínez-Ahumada, D. He, V. Berryman, A. López-Olvera, M. Hernandez, V. Jancik, V. Martis, M. A. Vera, E. Lima, D. J. Parker, A. I. Cooper, I. A. Ibarra and M. Liu, *Angew. Chem., Int. Ed.*, 2021, **60**, 17556–17563.
53 M. Y. S. Hamid, M. L. Firmansyah, S. Triwahyono, A. A. Jalil, R. R. Mukti, E. Febriyanti, V. Suendo, H. D. Setiabudi, M. Mohamed and W. Nabgan, *Appl. Catal., A*, 2017, **532**, 86–94.
54 H. Wang and F. Shadman, *AIChE J.*, 2013, **59**, 1502–1510.
55 L. Gang, H. Shaoguang and K. Qian, *Silicon*, 2022, **14**, 2225–2233.
56 Á. A. Beltrán-Osuna, J. L. Gómez Ribelles and J. E. Perilla, *J. Nanopart. Res.*, 2017, **19**, 381.
57 Y. Chen, X. Shi, B. Han, H. Qin, Z. Li, Y. Lu, J. Wang and Y. Kong, *J. Nanosci. Nanotechnol.*, 2012, **12**, 7239–7249.
58 M. Thommes, K. Kaneko, A. V. Neimark, J. P. Olivier, F. Rodriguez-Reinoso, J. Rouquerol and K. S. W. Sing, *Pure Appl. Chem.*, 2015, **87**, 1051–1069.
59 F. Ariffin, S. M. Izan, A. A. Jalil, C. R. Mamat, N. Basar, J. Jaafar, H. Hamdan and S. Triwahyono, *Malaysian J. Catal.*, 2017, **2**, 86–90.
60 M. Y. Shahul Hamid, S. Triwahyono, A. A. Jalil, N. W. Che Jusoh, S. M. Izan and T. A. Tuan Abdullah, *Inorg. Chem.*, 2018, **57**, 5859–5869.
61 T. C. Drage, C. E. Snape, L. A. Stevens, J. Wood, J. Wang, A. I. Cooper, R. Dawson, X. Guo, C. Satterley and R. Irons, *J. Mater. Chem.*, 2012, **22**, 2815–2823.
62 L. H. Macfarlan, M. T. Phan and R. Bruce Eldridge, *Chem. Eng. Sci.*, 2023, **275**, 118720.
63 J. A. Delgado, M. A. Uguina, J. L. Sotelo and B. Ruíz, *Sep. Purif. Technol.*, 2006, **49**, 91–100.
64 H. Ning, R. Tang, C. Li, X. Gu, Z. Gong, C. Zhu, J. Li, K. Wang and J. Yu, *Sep. Purif. Technol.*, 2025, **353**, 128425.
65 A. N. Módenes, F. B. Scheufele, F. R. Espinoza-Quiñones, P. S. Carraro de Souza, C. R. B. Cripa, J. Dos Santos, V. Steffen and A. D. Kroumov, *Int. J. Bioautomotion*, 2015, **19**, 187–206.
66 S. Tazikeh, A. Shafiei, T. Yerkenov, A. Abenov, N. Seitmaganbetov and T. Sh. Atabaev, *Fuel*, 2022, **329**, 125379.
67 G. Avijegon, G. Xiao, G. Li and E. F. May, *Adsorption*, 2018, **24**, 381–392.
68 J. H. Carter, X. Han, F. Y. Moreau, I. da Silva, A. Nevin, H. G. W. Godfrey, C. C. Tang, S. Yang and M. Schröder, *J. Am. Chem. Soc.*, 2018, **140**, 15564–15567.
69 T. Hou, W. Zeng and Q. Zhou, *Chemosensors*, 2022, **10**, 279.
70 Y. Song, J. Cheng, Y. Miao, W. Guo and J. Zhou, *ACS Sustainable Chem. Eng.*, 2021, **9**, 5580–5589.
71 H. Wang, J. Li and Z. Zhang, *Nanomaterials for Carbon Dioxide Capture and Conversion Technologies*, Elsevier, 2023, pp. 261–275.

72 J. Zhou, J. Ma and Z. Wang, *Fuel Process. Technol.*, 2022, **227**, 107133.
73 G. Cui, S. Lyu, F. Zhang, H. Wang, Z. Li, Y. Li and J. Wang, *Ind. Eng. Chem. Res.*, 2020, **59**, 21522–21529.
74 H. Mashhadimoslem, M. Safarzadeh Khosrowshahi, M. Jafari, A. Ghaemi and A. Maleki, *ACS Omega*, 2022, **7**, 18409–18426.
75 M. K. A. Asman, N. A. Lutpi, Y. Wong, M. A. Hanif, S. Ong, F. A. Dahalan, N. I. Iberahim and M. Hamdzah, *Environ. Quality Manage.*, 2024, **33**, 81–89.
76 N. Ahmad, N. Ibrahim, P. Yun Fu and R. Ahmad, *J. Teknol.*, 2020, **82**(5), 127–133.
77 X. Zhang, H. Xu, W. Xiang, X. You, H. Dai and B. Gao, *Biochar*, 2024, **6**, 22.
78 B.-C. Alcántar-Vázquez and R.-M. Ramírez-Zamora, *Adsorption*, 2020, **26**, 687–699.
79 B. Guo, Y. Wang, X. Shen, X. Qiao, L. Jia, J. Xiang and Y. Jin, *Materials*, 2020, **13**, 877.
80 F. Raganati, M. Alfe, V. Gargiulo, R. Chirone and P. Ammendola, *Chem. Eng. J.*, 2019, **372**, 526–535.
81 J. Wang and X. Guo, *J. Hazard. Mater.*, 2020, **390**, 122156.
82 D. Tiwari, C. Goel, H. Bhunia and P. K. Bajpai, *Sep. Purif. Technol.*, 2017, **181**, 107–122.
83 B. Li and C. Ma, *Energy Proc.*, 2018, **153**, 471–477.
84 R. Serna-Guerrero and A. Sayari, *Chem. Eng. J.*, 2010, **161**, 182–190.
85 Y. Liu and X. Yu, *Appl. Energy*, 2018, **211**, 1080–1088.
86 Y. Chen, J. Wu, X. Wang, M. Liu and Y. Liu, *Molecules*, 2022, **27**, 3429.
87 J. Rojas, D. Suarez, A. Moreno, J. Silva-Agredo and R. A. Torres-Palma, *Appl. Sci.*, 2019, **9**, 5337.
88 Y. Liu and X. Yu, *Appl. Energy*, 2018, **211**, 1080–1088.
89 Q. Zhang, J. Wei, C. Gao, Y. Zheng, Y. Xiao, F. Liu and L. Jiang, *J. Cleaner Prod.*, 2024, **436**, 140633.
90 H. Deng, H. Yi, X. Tang, Q. Yu, P. Ning and L. Yang, *Chem. Eng. J.*, 2012, **188**, 77–85.
91 M. Ghaedi, A. G. Nasab, S. Khodadoust, M. Rajabi and S. Azizian, *J. Ind. Eng. Chem.*, 2014, **20**, 2317–2324.
92 A. A. A. Darwish, M. Rashad and H. A. AL-Aoh, *Dyes Pigm.*, 2019, **160**, 563–571.
93 A. A. El-Bindary, A. Z. El-Sonbati, A. A. Al-Sarawy, K. S. Mohamed and M. A. Farid, *Spectrochim. Acta, Part A*, 2015, **136**, 1842–1849.
94 S. Yang, L. Li, Z. Pei, C. Li, J. Lv, J. Xie, B. Wen and S. Zhang, *Colloids Surf., A*, 2014, **457**, 100–106.
95 S. Banerjee, G. C. Sharma, M. C. Chattopadhyaya and Y. C. Sharma, *J. Environ. Chem. Eng.*, 2014, **2**, 1870–1880.